Structure, electronic and magnetic characterization, and calculated electronic structures of two oxyhalide hexagonal perovskites

L. T. Nguyen, X. Gui, H. E. Mitchell Warden, and R. J. Cava

Phys. Rev. Materials **5**, 104408 — Published 19 October 2021
DOI: 10.1103/PhysRevMaterials.5.104408

Structure, Elementary Electronic and Magnetic Properties and Calculated Electronic Structures of Two Oxyhalide Hexagonal Perovskites

L.T. Nguyen, X. Gui, H.E. Mitchell Warden, and R.J. Cava

Department of Chemistry, Princeton University, Princeton NJ 08540

ABSTRACT

We report the crystal structures, initial magnetic and charge transport characterization, and calculated electronic structures of the hexagonal oxyhalide perovskites, $Ba_7Ru_4O_{15}Cl_2$ and $Ba_7Ru_4O_{15}Br_2$. The experimental information is obtained through the study of single crystals. Face-sharing RuO_6 octahedra form Ru_2O_9 dimers in a layered triangular geometry in these materials; minor amounts of off-magnetic-site structural disorder are present in our crystals. Both are magnetically isotropic, with 2.5 µB/mol-Ru, Curie-Weiss theta -185 K, and 2.9 µB/mol-Ru, Curie-Weiss theta -168 K, respectively. Broad features in the magnetic susceptibility and heat capacity associated with magnetic ordering (at 35 and 37 K, respectively) are observed. The charge transport band gaps are 0.03 eV for the oxychloride and 0.006 eV for the oxybromide. There is no gap at the Fermi level for either of these compounds in Density Functional Theory (DFT) electronic structure calculations.

Keywords: hexagonal oxyhalide perovskite, face-sharing octahedra, magnetic ruthenates, short-range ordering, DFT calculations.

INTRODUCTION

Ruthenates often display interesting magnetic and electronic properties[1]. Although $SrRuO_3$ and $CaRuO_3$ are nominally isostructural, for example, $SrRuO_3$ displays a ferromagnetic transition at Tc=165 K while $CaRuO_3$ remains paramagnetic down to 2 K[2-4]. The discovery of superconductivity in Sr_2RuO_4 at 1.5 K has drawn a substantial amount of attention [5] and ruthenates such as $BaRuO_3$ also display unusual properties[6–13]. To compliment what is known about this class of materials, we here report the crystal structures and initial single crystal magnetic and electronic characterization of two dimer-based hexagonal oxyhalide perovskites, $Ba_7Ru_4O_{15}Cl_2$ and $Ba_7Ru_4O_{15}Br_2$. The crystal structures differ in a minor way from those that have been previously reported[14,15], as structural disorder is observed in our materials; the magnetic properties can be considered consistent with that disorder. We also describe their Density Functional Theory (DFT)-calculated electronic structures.

The growth of small crystals of $Ba_7Ru_4O_{15}Cl_2$ and $Ba_7Ru_4O_{15}Br_2$ has been previously reported[14,15], but we successfully grew crystals of a size and quality suitable for the characterization of the anisotropic magnetic properties. For both materials, the magnetic susceptibilities are isotropic from 300 K down to around 40 K. The effective magnetic moments are approximately 2.5 µB/mol-Ru in the oxychloride and 2.9 µB/mol-Ru in the oxybromide. The Curie-Weiss temperatures are approximately -185 K and -168 K, respectively. Using these calculated Curie-Weiss temperatures, the exchange interaction constants [16–18] (J/k_B) are estimated to be quite similar in the two materials, 125 K for $Ba_7Ru_4O_{15}Cl_2$ and 113 K for $Ba_7Ru_4O_{15}Br_2$. Broad peaks are observed in the magnetic susceptibility and heat capacity, at 35 K for $Ba_7Ru_4O_{15}Cl_2$ and 37 K for $Ba_7Ru_4O_{15}Br_2$, suggesting the presence of short-range or low dimensional magnetic ordering. The transport band gaps are 0.03 eV and 0.006 eV, respectively.

These small band gaps imply that both materials are at the edge of metallic behavior. Finally, there is no gap at the Fermi level for either of these compounds seen in the Density-Functional-Theory-based electronic structure calculations.

EXPERIMENT

Materials Synthesis Single crystals of $Ba_7Ru_4O_{15}Cl_2$ and $Ba_7Ru_4O_{15}Br_2$ were synthesized by a flux growth method. $BaCO_3$ (dried in the oven at 120°C for 3 days), RuO_2 (Alfa Aesar, 99.95%), and $BaCl_2.2H_2O$ or $BaBr_2.2H_2O$ (Alfa Aesar, 99.9%) were mixed stoichiometrically and ground well with $BaCl_2.2H_2O$ or $BaBr_2.2H_2O$ flux media in a mass ratio of 1:3. The starting materials were placed in a alumina crucible, heated in air to 1000°C at the rate of 180°C/hr., held for 5 hours, and then cooled at a rate of 0.5°C/hr. to 800°C, after which they were cooled to room temperature at the rate 180°C/hr. The black hexagonal plate crystals obtained were separated from the flux by placing the resulting mass in water, sonicating and finally washing with ethanol. The black hexagonal crystals have a layered morphology. The crystals of both materials can easily be cleaved along the (001) plane, facilitating the single crystal characterization.

Single-Crystal X-Ray Diffraction Measurements and Refinements The crystal structures were determined by single-crystal X-ray diffraction. The diffraction data were collected at 293 K with a Kappa Apex2 CCD diffractometer (Bruker) using graphite-monochromated Mo-Kα radiation ($\lambda = 0.71073$ Å). The raw data were corrected for background, polarization, and Lorentz factor, and multiscan absorption corrections were applied. Finally, the structures were analyzed by the Intrinsic Phasing method provided by the ShelXL structure solution program. The structure solution was carried out by using direct methods and full-matrix least-squares on F^2 with the SHELXTL package. The crystal structure drawings were created by using the program VESTA[19].

Temperature-dependent Magnetization, Resistivity, and Thermodynamic Measurements Relatively large single crystals, up to 1.5 mm in maximum hexagonal plate dimension for $Ba_7Ru_4O_{15}Cl_2$ and 3 mm for $Ba_7Ru_4O_{15}Br_2$, were used for the magnetization measurements. The dc magnetic susceptibilities were measured in a Quantum Design Physical Property Measurement System (PPMS) DynaCool. The magnetic susceptibility was defined as M/H, where M is the sample magnetization in emu and H is the applied field in Oe. Temperature-dependent susceptibilities were measured in a field of $\mu_0H = 1$ Tesla. (M vs. μ_0H was linear to applied fields of 9 Tesla at all measurement temperatures). The resistivity in the hexagonal plane was measured by a dc four-contact method in the temperature range 50 to 300 K in the PPMS. Four Pt contact wires were connected to crystals using silver paint. The heat capacity was measured on single crystals from 1.8 to 80 K in the PPMS.

DFT Calculations Electronic structure calculations for $Ba_7Ru_4O_{15}Cl_2$ and $Ba_7Ru_4O_{15}Br_2$ were performed with the Vienna ab initio Simulation Package (VASP)[20–23] using the projector-augmented wave (PAW)[24,25] method and the generalized gradient approximation (PBE-GGA)[26]. The density of states (DOS) curves and band structures for each compound were generated via a two-step process. First, we performed a static self-consistent calculation to obtain the DOS and a converged charge density. The charge density was then used in a non-self-consistent calculation along a high-symmetry path of the Brillouin zone (BZ), resulting in the band structure. The experimental AFM structures, with further relaxation to exclude any structural disorder, were used in the calculations. The energy cut-off was set to 500 eV with convergence criteria of 1×10^{-5} eV. For the DOS curve, a Γ−centered Monkhorst-Pack 6 × 6 × 6 *k*-point mesh was used. The band structure was calculated along the following path of the BZ, with 39 *k*-points connecting each special point: $\Gamma-L-B_1|B-Z-\Gamma-X|Q-F-P_1-Z|L-P$[27]. Spin-orbit coupling was included.

RESULTS and DISCUSSION

Crystal structure Both $Ba_7Ru_4O_{15}Cl_2$ and $Ba_7Ru_4O_{15}Br_2$ crystallize in a centrosymmetric rhombohedral structure, in space group *R*-3*m* (No. 166). The structural parameters determined by single crystal refinements are presented in **Table 1** and **Table 2**. The crystal structures of our materials are slightly different from those in previous reports[14,15] as shown in **Figure 1a**. In our structural analysis, minor amounts of structural disorder are seen for one Ba-site and an associated Cl/Br site – in the non-magnetic Ba-O-Cl layers - the Ba ion in the "normal" (Ba3) site, with its dominant occupancy of around 90% in $Ba_7Ru_4O_{15}Cl_2$ and 94% $Ba_7Ru_4O_{15}Br_2$, can bond with either Cl8/Br8 or Cl9/Br9, while the "defect" Ba ion in the Ba4 site, with its minor occupancy of around 10% in $Ba_7Ru_4O_{15}Cl_2$ and 6% $Ba_7Ru_4O_{15}Br_2$, can only bond with Cl9/Br9. The occupancies of these sites are constrained so the overall stoichiometric formula of $Ba_7Ru_4O_{15}X_2$ (X=Cl, Br) is maintained, as summarized in **Table 2**. The reason that this structural disorder was not reported for previously grown crystals is not known, but it is known that off-site disorder can impact the magnetic properties of frustrated materials[28–30]. Directly relevant to the magnetic properties, the magnetic Ru_2O_9 dimers are arranged in a triangular planar lattice with a relatively large plane-to-plane distance.

The structure-property relationships in these materials are of interest. The magnetic exchange interactions present depend on both the metal-metal distances and the metal-oxygen orbital overlap. Within the Ru_2O_9 dimers, which are made from face-sharing RuO_6 octahedra, the short Ru-Ru distances, 2.73 Å in $Ba_7Ru_4O_{15}Cl_2$ and 2.72 Å in $Ba_7Ru_4O_{15}Br_2$, suggest that there are strong metal-metal interactions between the Ru ions. One RuO_6 octahedron in each dimer is nearly ideal in shape while the other shows a distortion, with two sets of different Ru-O bond lengths: the distorted octahedron is closer to the Ba_2Cl_2 double layer than the more ideal one. Some selected bond lengths in both $Ba_7Ru_4O_{15}Cl_2$ and $Ba_7Ru_4O_{15}Br_2$ are summarized in **Table 3**.

Magnetic susceptibility. Figure 2 shows the temperature-dependent dc magnetic susceptibility for $Ba_7Ru_4O_{15}Cl_2$ down to 1.8 K. The Curie-Weiss fit to the data from 100 to 300 K results in $\Theta_{CW,\perp}$ = -191 K, $\mu_{eff,\perp}$ = 2.54 uB/mol-Ru and $\Theta_{CW,\parallel}$ = -179 K, $\mu_{eff,\parallel}$ = 2.53 uB/mol-Ru for applied magnetic fields perpendicular or parallel to the *c*-axis, respectively. The negative Curie-Weiss temperatures observed indicate the dominance of antiferromagnetic interactions - the overall exchange interaction constant J/k_B is estimated to be 125 K. The material appears to be relatively isotropic magnetically. Short-range magnetic ordering or low dimensional ordering is seen at around 35 K, evidenced by broad humps in both the magnetic susceptibility (**Figure 2**) and heat capacity (**Figure 4b**). The field-dependent magnetization, measured up to 9 Tesla (Insets in **Figure 2**) shows no indication of magnetic saturation in either direction down to 2 K.

A similar analysis of the $Ba_7Ru_4O_{15}Br_2$ magnetic susceptibility is shown in **Figure 3**. The Curie-Weiss fits of the data from 100 to 300 K result in $\Theta_{CW,\perp}$ = -173 K, $\mu_{eff,\perp}$ = 2.91 uB/mol-Ru and $\Theta_{CW,\parallel}$ = -163 K, $\mu_{eff,\parallel}$ = 2.82 uB/mol-Ru. Similar to the case of $Ba_7Ru_4O_{15}Cl_2$, strong antiferromagnetic interactions are reflected by the large negative Curie-Weiss temperatures. There is no sign of magnetic saturation up to 9 Tesla at 2 K. From the calculated Curie-Weiss temperatures, the exchange interaction constant J/k_B is estimated to be 113 K in $Ba_7Ru_4O_{15}Br_2$.

When comparing the magnetism of the current materials to that of a material based on similar Ru_2O_9 dimers with the same number of electrons per dimer, i.e. $Ba_3InRu_2O_9$, both $Ba_7Ru_4O_{15}Cl_2$ and $Ba_7Ru_4O_{15}Br_2$ show a larger effective magnetic moment. In a similar formally mixed spin state of Ru^{4+} and Ru^{5+} ions, $Ba_3InRu_2O_9$ exhibits a spin glass transition at 3.5 K and its spin ½ moment is delocalized in the Ru_2O_9 dimers, which has been attributed to the strong ruthenium-oxygen orbital hybridization[31,32]. The current materials magnetically order at a temperature a factor of 10 larger, consistent with their much larger effective moments. These differences support the conclusion that the magnetism of the Ru_2O_9 dimers is significantly impacted by the remainder of the crystal structure even when the electron count per dimer is the same.[32] At a different electron count per dimer, but similar in that it is based on magnetic Ru_2O_9 dimers, $Ba_3NaRu_2O_9$ has an effective moment of 0.46 μB/mol-Ru and remains paramagnetic down to 1.7 K[33]. Thus the electron count per dimer is a likely a significant factor as well.

Figure 4a shows the normalized temperature dependence of the normalized magnetic susceptibility ($C/\chi|\Theta| = T/|\Theta|+1$), a type of plot that normalizes the data of individual materials to the magnetic interaction temperature (Θ) and the size of the observed moment (C), facilitating the comparison of different materials[34–36]. Ideal Curie-Weiss behavior in a material yields a straight line with a slope of 1 and a *y*-intercept of either 1 or -1 in the case of dominant AFM or FM interactions, and magnetic ordering near $T/|\Theta| = 1$. We use it in this case to compare $Ba_7Ru_4O_{15}Cl_2$ to $Ba_7Ru_4O_{15}Br_2$. For the current materials, for values of $T/|\Theta|$ larger than 0.4, both compounds follow ideal Curie-Weiss paramagnetic behavior (green dashed line). The positive deviations in the normalized susceptibilities for $T/|\Theta|$ below 0.4 indicate the presence of antiferromagnetic short-range correlations in addition to those expected for an ordinary antiferromagnet, and the strong upturns reflect the magnetic ordering, which is relatively broad in both cases. The behaviors of the two materials are quite similar.

Heat capacity. Figure 4b shows the heat capacity data as a function of temperature for both materials. The broad humps at 35 K for $Ba_7Ru_4O_{15}Cl_2$ and 37 K for $Ba_7Ru_4O_{15}Br_2$ agree well with the antiferromagnetic magnetic ordering observed in the magnetic susceptibility in **Figure 2** and **Figure 3**. The Sommerfeld constants (the γ-terms) were determined from the extrapolation of the

Cp/T vs T^2 plots to intersect with the *y*-axis. As shown in the inset of **Figure 4b**, γ is found to be around 10 mJ/mol-K^2 in $Ba_7Ru_4O_{15}Cl_2$ and almost zero in $Ba_7Ru_4O_{15}Br_2$. The γ-terms, which are the sum of the electronic contribution to the total heat capacity and the core diamagnetism (normalized), indicate that the materials do not have heavy carriers near E_F and that the normalized density of electronic states is lower in $Ba_7Ru_4O_{15}Br_2$ than it is in $Ba_7Ru_4O_{15}Cl_2$.

Resistivity Both materials show weakly semiconducting behavior. A logarithmic representation of the temperature-dependent resistivity data for both materials is shown in **Figure 5;** the raw resistance data is outlined in the insets. The data can be fit to the standard model: $\rho = \rho_0 e^{E_a/k_B T}$ with an activation energy E_a of 0.03 eV in $Ba_7Ru_4O_{15}Cl_2$ and 0.006 eV in $Ba_7Ru_4O_{15}Br_2$ (**Figure 5**). These small band gaps indicate that both materials are on the edge of being metallic. How the small but detectable amount of structural disorder observed impacts the transport properties is not understood.

DFT calculations The results of the electronic structure calculations are presented in **Figure 6**. The density of states (DOS) curve for $Ba_7Ru_4O_{15}Cl_2$ (**Figure 6a**) shows a small number of states, at the Fermi energy (E_F). A similar situation can be seen for $Ba_7Ru_4O_{15}Br_2$, but there also appears to be a small energy range slightly above E_F where the DOS goes to zero (**Figure 6b**). The highest energy occupied states and lowest energy unoccupied states are calculated to be dominated by Ru 4*d* orbitals. The results of the calculations contrast with the minor semiconducting behavior observed experimentally, though the tendency of DFT to underestimate band gaps provides a potential explanation for the discrepancy. In **Figure 6**, we show the band structures for these two compounds. In each case, the *k*-point path along the primitive Brillouin zone is the same (Γ−L−B_1|B−Z− Γ−X|Q−F−P_1−Z|L−P) and the similarities of these compounds becomes quite apparent. Along B−Z− Γ−X, the valence band maximum (VBM) crosses E_F and becomes of nearly equal energy to the conduction band minimum (CBM) at other points in the structure. These relatively small overlaps of the VBM-CBM support the experimental results that suggest that these compounds are at semiconductors with very small band gaps.

CONCLUSIONS

$Ba_7Ru_4O_{15}Cl_2$ and $Ba_7Ru_4O_{15}Br_2$, grown by the flux growth method, crystallize in a hexagonal perovskite unit cell in space group *R*-3*m*. The crystal structure consists of two face-sharing RuO_6 octahedra forming Ru_2O_9 dimers in a layered triangular geometry. Both materials are magnetically isotropic with large negative Curie-Weiss temperatures, indicating the dominance of antiferromagnetic interactions. The broad humps observed in the magnetic susceptibility and heat capacity for both materials imply that there is magnetic ordering at 35 K in $Ba_7Ru_4O_{15}Cl_2$ and 37 K in $Ba_7Ru_4O_{15}Br_2$. The small band gaps in the transport measurements suggest that both materials may be at the edge of metallic behavior; the observed semiconducting behavior is not reproduced in the DFT calculations performed. Future work may reveal that theoretically estimated J’s may or may not be directly comparable to those obtained experimentally, but at least they can be compared for the materials described in this work. We conclude that the combined theoretical and experimental data that we have obtained suggests that doping of these materials may lead to the discovery of a metallic conductor in the complex hexagonal perovskite family.

ACKNOWLEDGMENTS

This work was supported by the Basic Energy Sciences Division of the US Department of Energy, grant DE-FG02-98ER45706.

REFERENCES

[1] D.I. Khomskii and G.A. Sawatzky, Solid State Commun. **102**, 87 (1997).

[2] H.T. Dang, J. Mravlje, A. Georges, and A.J. Millis, Phys. Rev. B - Condens. Matter Mater. Phys. **91**, 1 (2015).

[3] G. Koster, L. Klein, W. Siemons, G. Rijnders, J.S. Dodge, C.B. Eom, D.H.A. Blank, and M.R. Beasley, Rev. Mod. Phys. **84**, 253 (2012).

[4] J.S. Lee, Y.S. Lee, T.W. Noh, K. Char, J. Park, S.-J. Oh, J.-H. Park, C.B. Eom, T. Takeda, and R. Kanno, Phys. Rev. B **64**, 245107 (2001).

[5] Y. Maeno, S. Kittaka, T. Nomura, S. Yonezawa, and K. Ishida, J. Phys. Soc. Japan **81**, 011009 (2012).

[6] Y.A. Ying, Y. Liu, T. He, and R.J. Cava, Phys. Rev. B **84**, 233104 (2011).

[7] M. V. Rama Rao, V.G. Sathe, D. Sornadurai, B. Panigrahi, and T. Shripathi, J. Phys. Chem. Solids **62**, 797 (2001).

[8] P.C. Donohue, L. Katz, and R. Ward, Inorg. Chem. **4**, 306 (1965).

[9] C.-Q.Q. Jin, J.-S.S. Zhou, J.B. Goodenough, Q.Q. Liu, J.G. Zhao, L.X. Yang, Y. Yu, R.C. Yu, T. Katsura, A. Shatskiy, and E. Ito, Proc. Natl. Acad. Sci. U. S. A. **105**, 7115 (2008).

[10] S.T. Hong and A.W. Sleight, J. Solid State Chem. **128**, 251 (1997).

[11] J.G. Zhao, L.X. Yang, Y. Yu, F.Y. Li, R.C. Yu, Z. Fang, L.C. Chen, and C.Q. Jin, J. Solid State Chem. **180**, 2816 (2007).

[12] A. Santoro, I. Natali Sora, and Q. Huang, J. Solid State Chem. **151**, 245 (2000).

[13] J.G. Zhao, L. Yang, Y. Yu, F. Li, R. Yu, and C.Q. Jin, J. Solid State Chem. **182**, 1524 (2009).

[14] J. Wilkens and H. Müller-Buschbaum, Acta Chem. Scand. **45**, 812 (1991).

[15] N. Tancret, P. Roussel, and F. Abraham, J. Solid State Chem. **177**, 806 (2004).

[16] Z. Ma, J. Wang, Z.Y. Dong, J. Zhang, S. Li, S.H. Zheng, Y. Yu, W. Wang, L. Che, K. Ran, S. Bao, Z. Cai, P. Čermák, A. Schneidewind, S. Yano, J.S. Gardner, X. Lu, S.L. Yu, J.M. Liu, S. Li, J.X. Li, and J. Wen, Phys. Rev. Lett. **120**, (2018).

[17] Y. Li, G. Chen, W. Tong, L. Pi, J. Liu, Z. Yang, X. Wang, and Q. Zhang, Phys. Rev. Lett. **115**, (2015).

[18] R. Zhong, S. Guo, G. Xu, Z. Xu, and R.J. Cava, Proc. Natl. Acad. Sci. **116**, 14505 (2019).

[19] K. Momma and F. Izumi, J. Appl. Crystallogr. **44**, 1272 (2011).

[20] G. Kresse and J. Furthmüller, Phys. Rev. B - Condens. Matter Mater. Phys. **54**, 11169 (1996).

[21] G. Kresse, J.F.-C. materials science, and undefined 1996, Elsevier (n.d.).

[22] G. Kresse and J. Hafner, Phys. Rev. B **47**, 558 (1993).

[23] G. Kresse and J. Hafner, Phys. Rev. B **49**, 14251 (1994).

[24] P.E. Blöchl, Phys. Rev. B **50**, 17953 (1994).

[25] D. Joubert, Phys. Rev. B - Condens. Matter Mater. Phys. **59**, 1758 (1999).

[26] J.P. Perdew, K. Burke, and M. Ernzerhof, Phys. Rev. Lett. **77**, 3865 (1996).

[27] W. Setyawan and S. Curtarolo, Comput. Mater. Sci. **49**, 299 (2010).

[28] C. Booth, J. Gardner, G. Kwei, R. Heffner, F. Bridges, and M. Subramanian, Phys. Rev. B - Condens. Matter Mater. Phys. **62**, R755 (2000).

[29] A. Andreanov, J.T. Chalker, T.E. Saunders, and D. Sherrington, (n.d.).

[30] K.W. Plumb, H.J. Changlani, A. Scheie, S. Zhang, J.W. Krizan, J.A. Rodriguez-Rivera, Y. Qiu, B. Winn, R.J. Cava, and C.L. Broholm, Nat. Phys. **15**, 54 (2019).

[31] L. Shlyk, S. Kryukov, V. Durairaj, S. Parkin, G. Cao, and L.E. De Long, J. Magn. Magn. Mater. **319**, 64 (2007).

[32] D. Ziat, A.A. Aczel, R. Sinclair, Q. Chen, H.D. Zhou, T.J. Williams, M.B. Stone, A. Verrier, and J.A. Quilliam, Phys. Rev. B **95**, 184424 (2017).

[33] H. Samata, M. Kai, T. Uchida, M. Ohtsuka, G. Tanaka, S. Sawada, T. Taniguchi, and Y. Nagata, J. Alloys Compd. **350**, 77 (2003).

[34] B.C. Melot, J.E. Drewes, R. Seshadri, E.M. Stoudenmire, and A.P. Ramirez, J. Phys. Condens. Matter **21**, (2009).

[35] S.E. Dutton, C.L. Broholm, and R.J. Cava, J. Solid State Chem. **183**, 1798 (2010).

[36] S.E. Dutton, Q. Huang, O. Tchernyshyov, C.L. Broholm, and R.J. Cava, Phys. Rev. B **83**, 64407 (2011).

Tables:

Table 1. Single crystal refinement for $Ba_7Ru_4O_{15}Cl_2$ and $Ba_7Ru_4O_{15}Br_2$.

Refined Formula	$Ba_7Ru_4O_{15}Cl_2$	$Ba_7Ru_4O_{15}Br_2$
Temperature (K)	296 (2)	293 (2)
F.W. (g/mol)	1676.56	1765.48
Space group; Z	R -3 m; 3	R -3 m; 3
a (Å)	5.7746 (2)	5.7957 (3)
c (Å)	51.662 (2)	52.843 (3)
V (Å^3)	1491.9 (1)	1537.2 (2)
Extinction Coefficient	0.00024 (3)	0.00001 (2)
θ range (deg)	6.874-33.190	2.312-33.192
No. reflections; R_{int}	2656; 0.0162	7367; 0.0316
No. independent reflections	785	829
No. parameters	43	43
R_1: ωR_2 (I>2δ(I))	0.0223; 0.0531	0.0375; 0.0935
Goodness of fit	1.112	1.177
Diffraction peak and hole (e$^-$/ Å^3)	2.055; -2.261	5.392; -4.104

Table 2. Atomic coordinates and equivalent isotropic displacement parameters of $Ba_7Ru_4O_{15}Cl_2$ and $Ba_7Ru_4O_{15}Br_2$. (U_{eq} is defined as one-third of the trace of the orthogonalized U_{ij} tensor (Å^2)).

$Ba_7Ru_4O_{15}Cl_2$:

Atom	**Wyck.**	**Occ.**	***x***	***y***	***z***	***U**_{eq}*
Ba1	3*a*	1	0	0	0	0.0094 (1)
Ba2	6*c*	1	0	0	0.28572 (2)	0.0078 (1)
Ba3	6*c*	0.898 (4)	0	0	0.08412 (2)	0.0093 (2)
Ba4	6*c*	0.102 (4)	0	0	0.0934 (2)	0.0093 (2)
Ba5	6*c*	1	0	0	0.20232 (2)	0.0200 (1)
Ru6	6*c*	1	0	0	0.35387 (2)	0.0048 (1)
Ru7	6*c*	1	0	0	0.40667 (2)	0.0066 (1)
Cl8	6*c*	0.73 (1)	0	0	0.14217 (5)	0.0285 (9)
Cl9	18*h*	0.090 (3)	0.203 (2)	0.797 (2)	0.1487 (2)	0.0285 (9)
O10	18*h*	1	0.4952 (4)	0.5048 (4)	0.0909 (1)	0.0124 (6)

$Ba_7Ru_4O_{15}Br_2$:

Atom	**Wyck.**	**Occ.**	***x***	***y***	***z***	***U**_{eq}*
Ba1	3*a*	1	0	0	0	0.0097 (2)
Ba2	6*c*	1	0	0	0.28696 (2)	0.0079 (2)
Ba3	6*c*	0.94 (1)	0	0	0.08220 (6)	0.0093 (4)
Ba4	6*c*	0.06 (1)	0	0	0.0903 (9)	0.0093 (4)
Ba5	6*c*	1	0	0	0.20580 (2)	0.0244 (3)
Ru6	6*c*	1	0	0	0.35327 (2)	0.0048 (2)
Ru7	6*c*	1	0	0	0.40473 (2)	0.0062 (2)
Br8	6*c*	0.77 (1)	0	0	0.14234 (5)	0.048 (1)
Br9	18*h*	0.077 (3)	0.207 (3)	0.793 (3)	0.1485 (3)	0.048 (1)
O10	18*h*	1	0.4948 (6)	0.5052 (6)	0.0888 (1)	0.012 (1)

Table 3. Selected bond lengths in $Ba_7Ru_4O_{15}Cl_2$ and $Ba_7Ru_4O_{15}Br_2$.

	$Ba_7Ru_4O_{15}Cl_2$	**$Ba_7Ru_4O_{15}Br_2$**
Ru6-Ru7	2.7278(15) Å	2.7193(16) Å
Ru6-O11	1.9760(6) Å	1.9771(6) Å
Ru6-O12	1.979(3) Å	1.994(5) Å
Ru7-O10	1.856(3) Å	1.864(5) Å
Ru7-O12	2.111(3) Å	2.100(5) Å
Ba1-O11	2.88730(8) Å	2.89785(16) Å
Ba1-O12	2.949(3) Å	2.957(5) Å
Ba2-O10	2.818(4) Å	2.830(6) Å
Ba2-O11	2.9714(9) Å	2.9672(9) Å
Ba2-O12	2.8940(13) Å	2.904(3) Å
Ba3-O10	2.9089(17) Å	2.919(3) Å
Ba3-O12	2.713(3) Å	2.710(6) Å
Ba3-X8 (X = Cl, Br)	2.999(3) Å	3.178(5) Å
Ba4-O10	2.8906(18) Å	2.899(3) Å
Ba4-O12	3.087(9) Å	3.04(4) Å
Ba4-X9 (X = Cl, Br)	3.505(15) Å	3.71(5) Å

Table 4: Summary of the magnetism in $Ba_7Ru_4O_{15}Cl_2$ and $Ba_7Ru_4O_{15}Br_2$.

100-300 K fitting	$\mathbf{Ba_7Ru_4O_{15}Cl_2}$	$\mathbf{Ba_7Ru_4O_{15}Br_2}$
H ⊥ c	Θ_{CW} = -191 K μ_{eff} = 2.54 uB/mol-Ru	Θ_{CW} = -173 K μ_{eff} = 2.91 uB/mol-Ru
H // c	Θ_{CW} = -179 K μ_{eff} = 2.53 uB/mol-Ru	Θ_{CW} = -163 K μ_{eff} = 2.82 uB/mol-Ru
Coupling constant J/k_B	125	113
Magnetic ordering	35 K	37 K

Figure captions:

Figure 1: (a) Crystal structure of $Ba_7Ru_4O_{15}X_2$ (X=Cl, Br) from z = ¼ to z = ¾. (The disordered Ba4 is shown in orange and the disordered Cl9/Br9 is shown in blue). (b) and (c) Two Ru_2O_9 dimers (two face-sharing RuO_6 octahedra) corner-sharing to each other. The Ru-O bond lengths are labelled and the crystals are displayed.

Figure 2: (a) Temperature-dependent magnetic susceptibility and (b) its inverse in $Ba_7Ru_4O_{15}Cl_2$ at the applied field of 1 T. Insets: Field-dependent magnetization of $Ba_7Ru_4O_{15}Cl_2$ at 2 K and 300 K with the applied field parallel and perpendicular to the *c*-axis, respectively.

Figure 3: (a) Temperature-dependent magnetic susceptibility and (b) its inverse in $Ba_7Ru_4O_{15}Br_2$ at the applied field of 1 T. Inset: Field-dependent magnetization of $Ba_7Ru_4O_{15}Br_2$ at 2 K and 300 K with the applied field parallel and perpendicular to the *c*-axis, respectively.

Figure 4: (a) Normalization and comparison of the temperature-dependent susceptibilities of these two materials. (The dashed line represents ideal Curie-Weiss behavior). (b) Heat capacity data measured from 1.8-80 K under zero applied field. A broad hump at around 35 K in $Ba_7Ru_4O_{15}Cl_2$ and 37 K in $Ba_7Ru_4O_{15}Br_2$ indicates a short-range magnetic ordering or low dimensional ordering, previously observed in the magnetic susceptibility. Inset: Low temperature fittings result to the γ-term of zero in $Ba_7Ru_4O_{15}Br_2$ and 10 mJ/mol-K^2 in $Ba_7Ru_4O_{15}Cl_2$.

Figure 5: Fitting of the resistivity data to the Arrhenius equation results to the band gap of (a) 0.03 eV in $Ba_7Ru_4O_{15}Cl_2$ and (b) 0.006 eV in $Ba_7Ru_4O_{15}Br_2$. The insets show the raw resistance data.

Figure 6: (a-b) Density of states curves and (c-d) Band structures of $Ba_7Ru_4O_{15}Cl_2$ and $Ba_7Ru_4O_{15}Br_2$, respectively, plotted from the DFT calculations.

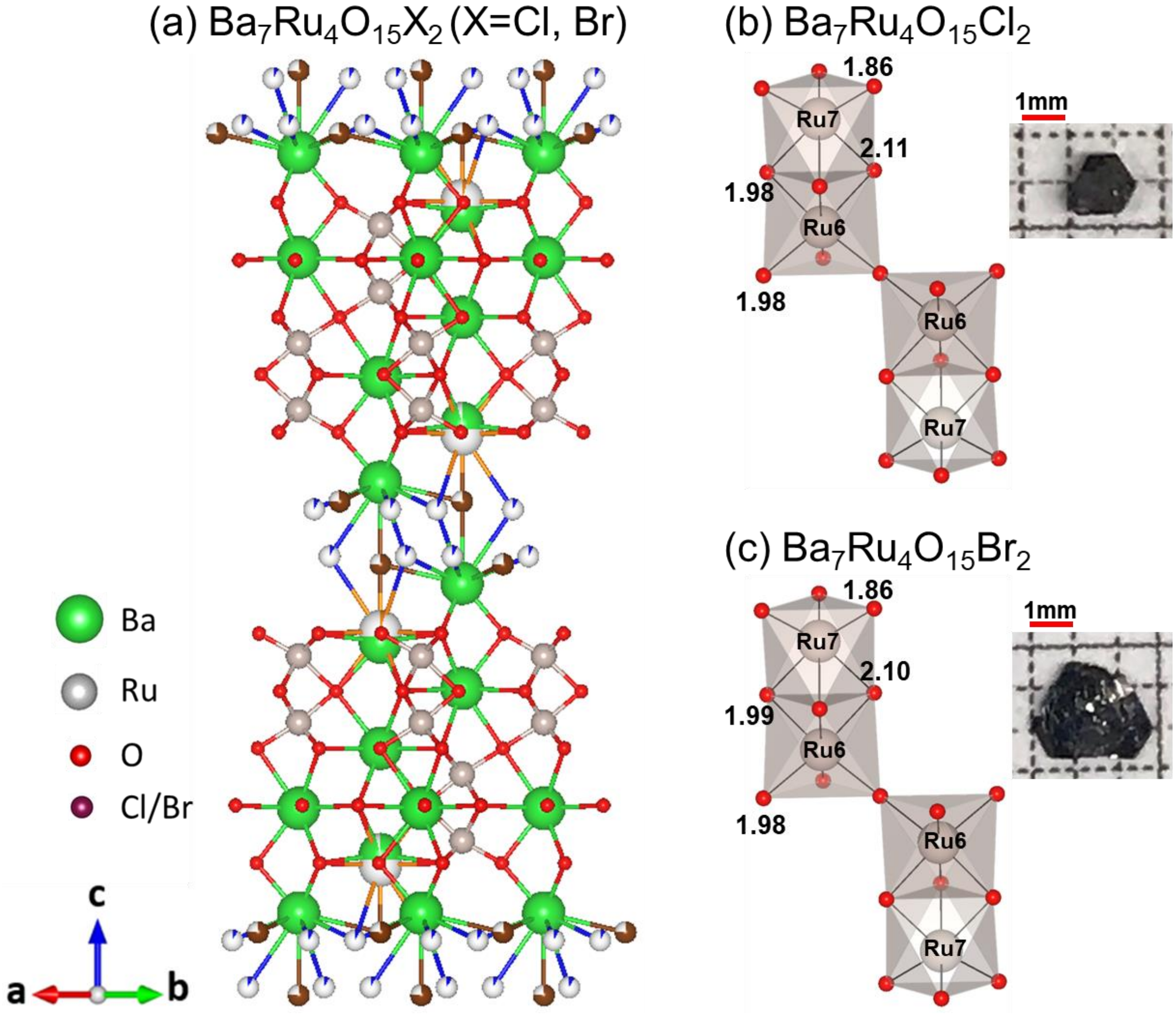

(a) $Ba_7Ru_4O_{15}X_2$ (X=Cl, Br)

(b) $Ba_7Ru_4O_{15}Cl_2$

(c) $Ba_7Ru_4O_{15}Br_2$

Figure 1.

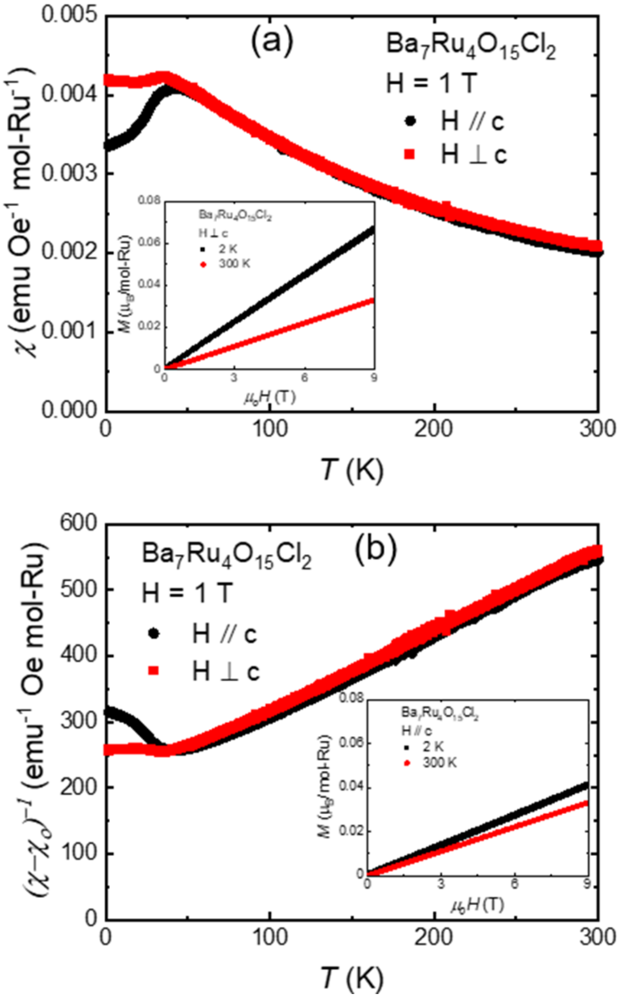
(a)
$Ba_7Ru_4O_{15}Cl_2$
H = 1 T
● H // c
■ H ⊥ c
χ (emu Oe^{-1} mol-Ru^{-1})
0.000
0.001
0.002
0.003
0.004
0.005
0
100
200
300
T (K)
$Ba_7Ru_4O_{15}Cl_2$
H ⊥ c
■ 2 K
● 300 K
M (μ_B/mol-Ru)
0
0.02
0.04
0.06
0.08
0
3
6
9
μ_0H (T)
(b)
$Ba_7Ru_4O_{15}Cl_2$
H = 1 T
● H // c
■ H ⊥ c
$(\chi-\chi_o)^{-1}$ (emu^{-1} Oe mol-Ru)
0
100
200
300
400
500
600
0
100
200
300
T (K)
$Ba_7Ru_4O_{15}Cl_2$
H // c
■ 2 K
● 300 K
M (μ_B/mol-Ru)
0
0.02
0.04
0.06
0.08
0
3
6
9
μ_0H (T)

Figure 2.

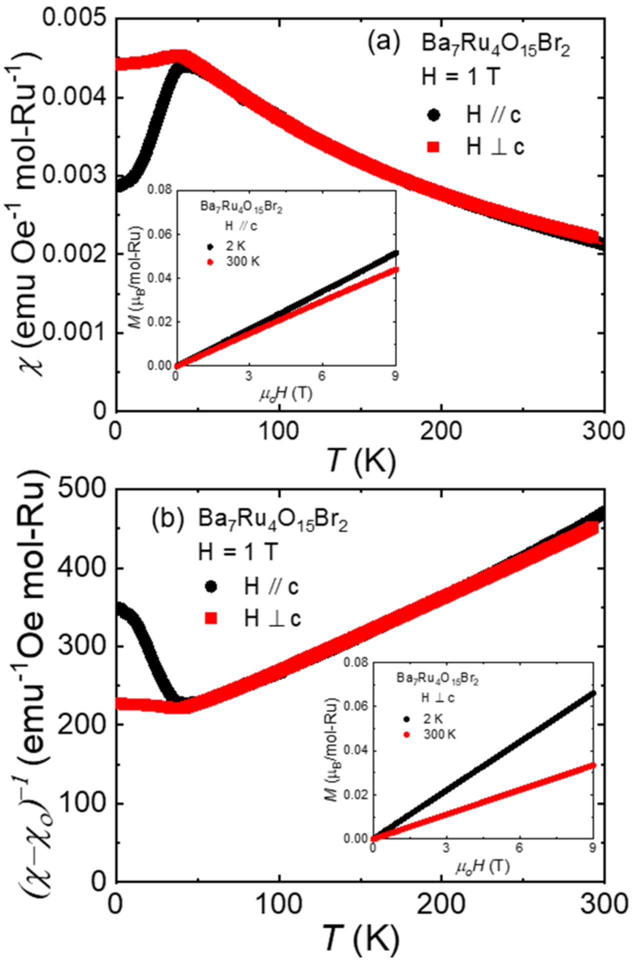
(a) Ba7Ru4O15Br2
H = 1 T
H // c
H ⊥ c
χ (emu Oe-1 mol-Ru-1)
0.005
0.004
0.003
0.002
0.001
0
T (K)
0
100
200
300
Ba7Ru4O15Br2
H // c
2 K
300 K
M (μB/mol-Ru)
0.08
0.06
0.04
0.02
0.00
μoH (T)
0
3
6
9
(b) Ba7Ru4O15Br2
H = 1 T
H // c
H ⊥ c
(χ−χo)-1 (emu-1Oe mol-Ru)
500
400
300
200
100
0
T (K)
0
100
200
300
Ba7Ru4O15Br2
H ⊥ c
2 K
300 K
M (μB/mol-Ru)
0.08
0.06
0.04
0.02
0.00
μoH (T)
0
3
6
9

Figure 3.

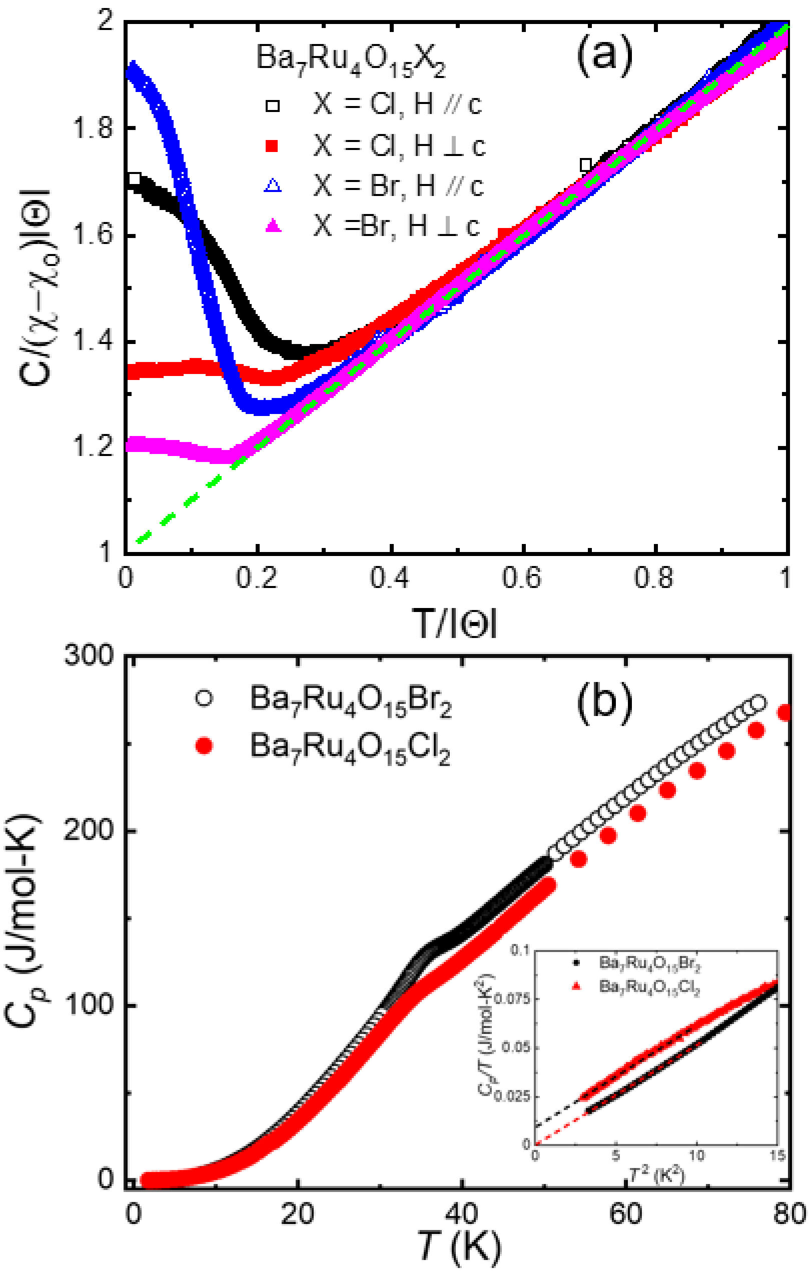
(a)
$Ba_7Ru_4O_{15}X_2$
X = Cl, H // c
X = Cl, H ⊥ c
X = Br, H // c
X =Br, H ⊥ c
$C/(\chi-\chi_o)|\Theta|$
2
1.8
1.6
1.4
1.2
1
0
0.2
0.4
0.6
0.8
1
$T/|\Theta|$
(b)
$Ba_7Ru_4O_{15}Br_2$
$Ba_7Ru_4O_{15}Cl_2$
C_p (J/mol-K)
300
200
100
0
0
20
40
60
80
T (K)
$Ba_7Ru_4O_{15}Br_2$
$Ba_7Ru_4O_{15}Cl_2$
C_p/T (J/mol-K^2)
0.1
0.075
0.05
0.025
0
0
5
10
15
T^2 (K^2)

Figure 4.

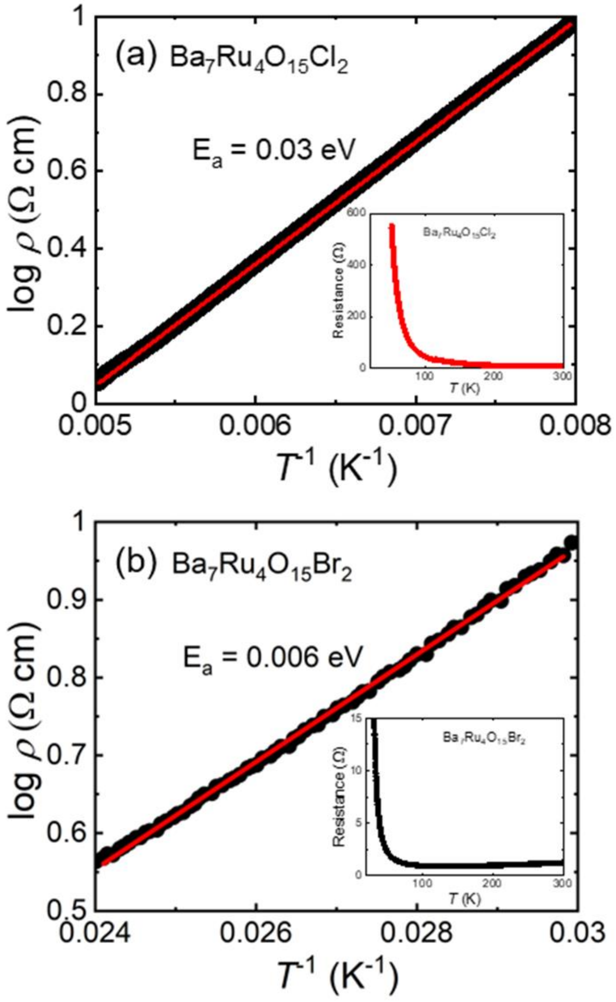
(a) Ba7Ru4O15Cl2
Ea = 0.03 eV
log ρ (Ω cm)
T-1 (K-1)
0
0.2
0.4
0.6
0.8
1
0.005
0.006
0.007
0.008
Ba7Ru4O15Cl2
Resistance (Ω)
T (K)
0
200
400
600
100
200
300
(b) Ba7Ru4O15Br2
Ea = 0.006 eV
log ρ (Ω cm)
T-1 (K-1)
0.5
0.6
0.7
0.8
0.9
1
0.024
0.026
0.028
0.03
Ba7Ru4O15Br2
Resistance (Ω)
T (K)
0
5
10
15
100
200
300

Figure 5.

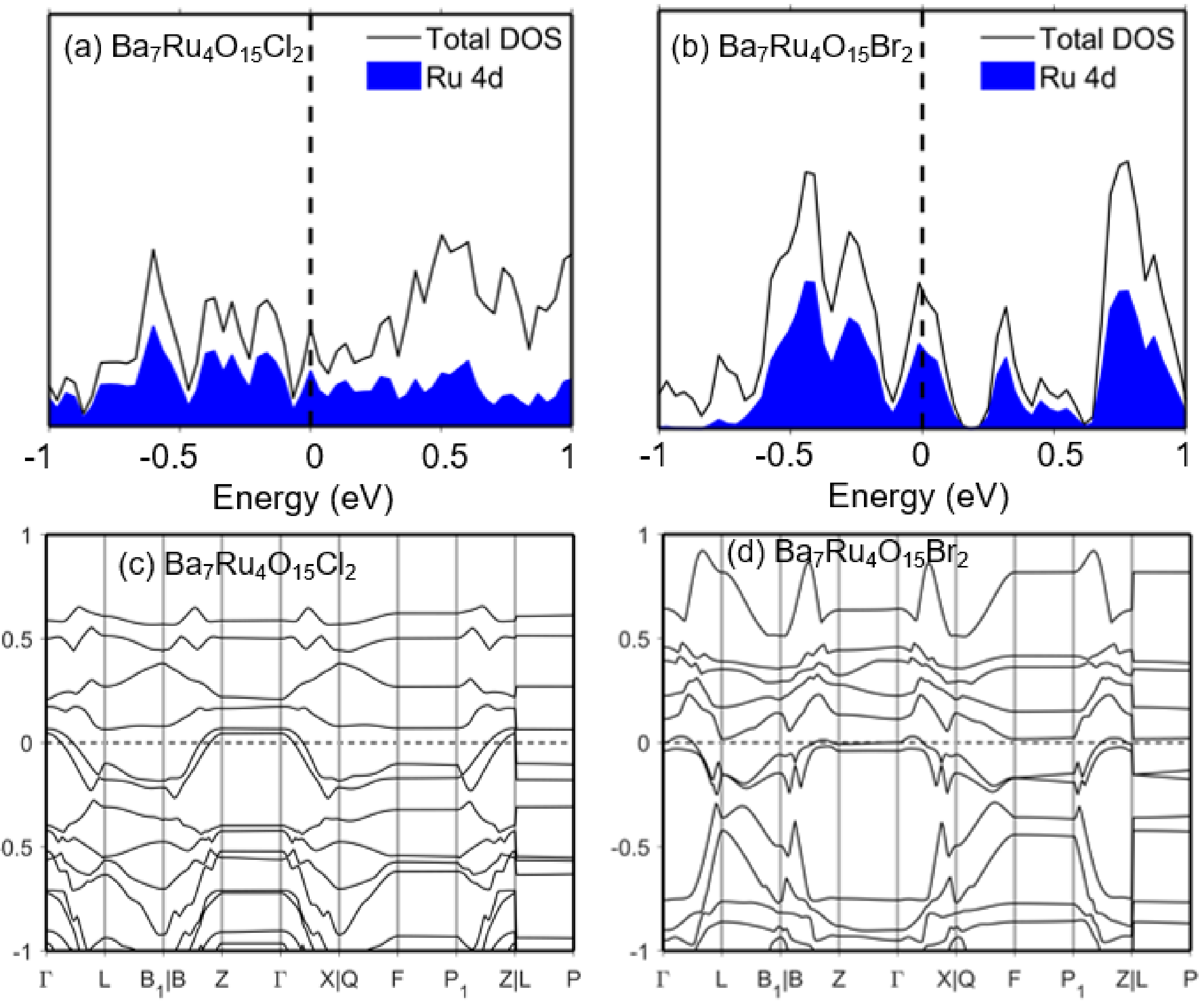
(a) Ba7Ru4O15Cl2
Total DOS
Ru 4d
-1
-0.5
0
0.5
1
Energy (eV)
(b) Ba7Ru4O15Br2
Total DOS
Ru 4d
-1
-0.5
0
0.5
1
Energy (eV)
(c) Ba7Ru4O15Cl2
1
0.5
0
-0.5
-1
Γ
L
B1|B
Z
Γ
X|Q
F
P1
Z|L
P
(d) Ba7Ru4O15Br2
1
0.5
0
-0.5
-1
Γ
L
B1|B
Z
Γ
X|Q
F
P1
Z|L
P

Figure 6.